Journal of Alloys and Compounds 867 (2021) 159030

Contents lists available at ScienceDirect

Journal of Alloys and Compounds

journal homepage: www.elsevier.com/locate/jalcom

Hierarchically porous silica supported ceria and platinum nanoparticles for catalytic combustion of toluene

Yu Hao[a], Shaohua Chen[a], Luming Wu[a], Rui Chen[a], Pingchuan Sun[b], Tiehong Chen[a,*]

[a] Institute of New Catalytic Materials Science, School of Materials Science and Engineering, Key Laboratory of Advanced Energy Materials Chemistry (MOE), Nankai University, Tianjin 300350, PR China
[b] Key Laboratory of Functional Polymer Materials (MOE), College of Chemistry, Nankai University, Tianjin 300071, PR China

ARTICLE INFO

Article history:
Received 17 November 2020
Received in revised form 28 January 2021
Accepted 31 January 2021
Available online 3 February 2021

Keywords:
Hierarchically porous
Toluene catalytic combustion
Pt nanoparticles
CeO_2 loading amount
Metal-support interaction

ABSTRACT

The hierarchically porous silica (NKM-5) was synthesized by the polyelectrolyte-surfactant mesomorphous complex templating method, and the NKM-5 was used as the carrier to load different amounts of ceria to prepare *x*Ce/NKM-5 samples (*x* represents the CeO_2 loading amount) by the impregnation method, and then supported Pt to prepare Pt/*x*Ce/NKM-5 catalyst for toluene catalytic combustion. NKM-5 sample has excellent specific surface area and pore structure, with the increase of CeO_2 loading amount, the specific surface area and pore volume of *x*Ce/NKM-5 sample decreased gradually. As the CeO_2 loading amount increased, XRD and TEM characterization showed that the Pt dispersion of Pt/*x*Ce/NKM-5 catalyst increased; XPS results showed that the proportion of Pt^0 decreased and the proportion of Ce^{3+} increased; H_2-TPR characterization showed that the reducibility increased; and the interaction between Pt and CeO_2 increased gradually. The toluene catalytic combustion activity of Pt/*x*Ce/NKM-5 catalyst first increased and then decreased with the increase of CeO_2 loading amount. Pt/30Ce/NKM-5 catalyst has the most excellent catalytic activity with 50% toluene conversion at 174 °C and 90% conversion at 195 °C, which is the result of the synergy effect of the hierarchical pore structure of the support and the metal-support interaction between Pt and CeO_2.

1. Introduction

Volatile organic compounds (VOCs) are those compounds with the melting point lower than room temperature and the boiling point between 50 and 260 °C under the normal temperature and pressure condition [1]. VOCs are considered to be the precursors of ozone, photochemical smog, secondary aerosols, PM 2.5, and other pollutants, which have a serious impact on global air pollution; in addition, it also has physiological toxicity, carcinogenesis, and teratogenic effects to the human body. Therefore, it is essential to reduce VOC emissions, among the available technologies, there are already adsorption [2], photocatalysis [3,4], plasma catalysis [5], catalytic combustion [6,7], and other technologies; catalytic combustion is the most promising technology due to its high efficiency, low energy consumption, and no secondary pollution [8].

The catalysts for catalytic combustion are mainly divided into noble metal catalysts [9–12] and non-noble metal catalysts [8,13]. Noble metal catalysts, especially Pt-based catalysts are widely used because they have excellent catalytic activity and durability [14–16]. Zeolite and mesoporous silica are widely used as the catalyst supports due to their excellent specific surface area and uniform pore size [17–20], but their small and single pore size limits the transport of reactants, so it is necessary to synthesize the hierarchical pore material that combines the advantages of various pore materials. When hierarchical pore materials are used as the catalyst supports, the diffusion efficiency of reactive molecules in the pores can be improved, thereby improving the transfer efficiency of substances in the catalytic process; in addition, the active species also can be well dispersed [21–23]. However, the support is generally an inert carrier and there is no interaction between the noble metal and the support, the dispersion of the precious metal is relatively low, and the precious metal nanoparticles are easy to agglomerate, resulting in relatively low catalytic activity, so it is necessary to introduce a substance that interacts with Pt to stabilize the Pt nanoparticles [24,25].

The ceria support has been widely used in various catalytic reactions due to its oxygen storage capacity, redox capacity, and strong metal-support interaction [26,27]. However, the specific surface area

* Corresponding author.
E-mail address: chenth@nankai.edu.cn (T. Chen).

https://doi.org/10.1016/j.jallcom.2021.159030
0925-8388/

and pore volume of ceria are very low [28,29], which limits the transfer of reactants and products; the particle size of ceria also affects its activity, by reducing the particle size of ceria, the contact area between noble metal and ceria can be increased, thereby promoting the interaction between them. One of the methods to reduce ceria is to load ceria on a carrier with large specific surface area [28,30–32], and then load the noble metal to achieve strong metal-support interaction.

The hierarchically porous silica NKM-5 was synthesized by the polyelectrolyte-surfactant mesomorphous complex templating method, the poly(acrylic acid) (PAA) as the anionic polyelectrolyte and hexadecyl pyridinium chloride (CPC) as the cationic surfactant; and the *x*Ce/NKM-5 (*x* represents the CeO_2 loading amount) samples with different CeO_2 loadings were synthesized by the impregnation method. The Pt/*x*Ce/NKM-5 catalyst was synthesized by the impregnation method and used for the catalytic combustion of toluene, the effects of different CeO_2 loading amounts on the physical properties, dispersity of Pt, valence state, and reduction ability were studied. In addition, the metal-support interaction between Pt and CeO_2, and the relationship with catalytic activity were also explored.

2. Experimental section

2.1. Materials

Hexadecyl pyridinium chloride (CPC, 99%), Tetraethyls orthosilicate (TEOS, >99%), Ethanol (CH_3CH_2OH, >99%), Cerium nitrate hexahydrate ($Ce(NO_3)_3.6H_2O$, 99.5% metal basis), Manganese nitrate tetrahydrate ($Mn(NO_3)_2.4H_2O$, 98%), tetrabutyl titanate (TBT, ≥99%) Chloroplatinic acid hexahydrate ($H_2PtCl_6.6H_2O$, Pt≥37.5%), Orthoboric acid (H_3BO_3, ACS), Nitric acid (HNO_3, 70%), Hydrofluoric acid (HF, ≥40%), and Cetyltrimethylammonium bromide (CTAB, 99%) were obtained from Aladdin. Poly(acrylic acid) (PAA) (average molecular weight 240,000, 25 wt% solution in water) was purchased from Alfa Aesar. Ammonium hydroxide solution ($NH_3{\cdot}H_2O$, 25–28%) was purchased from Macklin. Hydrochloric acid (HCl, 36–38%) was purchased from Tianjin Chemical Reagent Wholesale Company, China. Pluronic P123 ($EO_{20}PO_{70}EO_{20}$, average molecular weight 5800) was purchased from Sigma Aldrich. All the reagents were used without any further purification.

2.2. Catalyst preparation

Hierarchically porous silica (NKM-5) was synthesized under alkaline condition [33,34]. 1.08 g of CPC was dissolved in 50 mL of deionized water, and then 6.0 g of PAA was added at room temperature. After stirring for 40 min, 8.0 g of $NH_3{\cdot}H_2O$ was added to the above solution under vigorous stirring, after further stirring for 30 min, 4.16 g of TEOS was added. The mixture was stirred for 1 h, and finally transferred into a Teflon-lined steel autoclave for hydrothermal synthesis at 80 °C for 48 h. The product was centrifuged and washed with deionized water, dried at 60 °C for 12 h, and calcined in a muffle furnace at 550 °C for 6 h. The sample was denoted as NKM-5 [35]. NKM-5-0.3 was synthesized with 0.3 g PAA and other reaction conditions are the same.

The CeO_2-loaded samples were prepared by impregnation method. 0.3 g NKM-5 was dissolved in ethanol solution, and stirred at room temperature for 5 h, then an appropriate amount of $Ce(NO_3)_3.6H_2O$ was added, followed by stirring at room temperature for 5 h. Finally, the solvent was evaporated under 60 °C water bath, the product was dried at 80 °C for 12 h and calcined in a muffle furnace at 500 °C for 4 h. The samples were designated as *x*Ce/NKM-5 (*x* represents the loading of CeO_2, *x* = 20, 30, 40, and 50 wt%).

The $Ce(NO_3)_3.6H_2O$ was calcined in a muffle furnace at 500 °C for 4 h to prepare CeO_2.

The catalysts supported Pt (1 wt%) were prepared by impregnation method. 0.3 g NKM-5, *x*Ce/NKM-5, or CeO_2 was dissolved in ethanol solution, and stirred at room temperature for 5 h, then an appropriate amount of $H_2PtCl_6.6H_2O$ was added, followed by stirring at room temperature for 5 h. Finally, the solvent was evaporated under 60 °C water bath, the product was dried at 80 °C for 12 h, calcined in a muffle furnace at 400 °C for 2 h, and reduced at 300 °C for 2 h under 10% H_2/Ar. The catalysts were denoted as Pt/NKM-5, Pt/*x*Ce/NKM-5, and Pt/CeO_2.

The SBA-15 sample was prepared under strong acidic conditions [36]. 2.0 g of P123 was dissolved in the mixed solution of 15 g of H_2O and 60 g of 2 mol/L of HCl, and heated in a water bath at 35 °C. After the solution was uniformly mixed, 4.25 g of TEOS was added dropwise under stirring. After stirring for 20 h, the white emulsion was transferred into a Teflon-lined steel autoclave and then reacted in an oven at 80 °C for 2 days. The obtained product was filtered, washed to neutral, dried at 60 °C and calcined at 550 °C for 6 h. The obtained material was denoted as SBA-15.

The MCM-41 sample was synthesized based on the reference [37], 0.85 g of CTAB was dissolved in 200 mL of deionized water in a 60 °C oven, and then 17.2 g of $NH_3{\cdot}H_2O$ was added at room temperature under rapid stirring, 4.37 g of TEOS was added to the above homogeneous solution, after stirring for 10 min, the white emulsion was transferred into a Teflon-lined steel autoclave for hydrothermal synthesis at 80 °C for 2 h. The reaction product was separated by filtration, washed with water, dried at 120 °C and calcined at 550 °C for 6 h. The sample was denoted as MCM-41.

The preparation method of *x*Mn/NKM-5 (*x* represents the loading of MnO_2) was similar to that of *x*Ce/NKM-5. After NKM-5 was dispersed and stirred, $Ce(NO_3)_3.6H_2O$ was replaced with $Mn(NO_3)_2.4H_2O$. After stirred, evaporated, and dried, the product calcined in a muffle furnace at 400 °C for 5 h. The $Mn(NO_3)_2.4H_2O$ was calcined in a muffle furnace at 400 °C for 5 h to prepare MnO_2.

The preparation method of *x*Ti/NKM-5 (*x* represents the loading amount of TiO_2) is similar to that of *x*Ce/NKM-5, the difference is that the $Ce(NO_3)_3.6H_2O$ was replaced by tetrabutyl titanate (TBT), and then 2 mL H_2O was added, then stirred, evaporated, dried, and calcined in a muffle furnace at 550 °C for 6 h. A certain amount of TBT was added to the ethanol, stirred for 5 h, then 2 mL H_2O was added, then stirred, evaporated, dried, and finally calcined in a muffle furnace at 550 °C for 6 h. The sample was denoted as TiO_2.

The preparation method of Pt/MCM-41, Pt/SBA-15, Pt/NKM-5-0.3, Pt/*x*Mn/NKM-5, Pt/MnO_2, Pt/*x*Ti/NKM-5, and Pt/TiO_2 catalysts was the same as that of Pt/NKM-5. The loading amounts of Pt were 1%.

2.3. Characterization

X-ray diffraction (XRD) and small-angle XRD were performed with powder sample on the Rigaku Smart Lab 3 kW diffractometer (Cu K_α radiation), the tube voltage is 40 kV and the tube current is 40 mA.

N_2 adsorption-desorption isotherms were measured on the Micromeritics ASAP 2020 physisorption instrument. The specific surface area was calculated by the BET (Brunauer-Emmett-Teller) method, the pore size distribution and the pore volume were calculated by the BJH (Barrett-Joyner-Halenda) method.

The morphology of the carrier was observed by field emission scanning electron microscopy (FE-SEM, JSM-7800). The high resolution morphology and the elemental distribution of the catalysts were obtained by transmission electron microscope (TEM, JEM-2800) equipped with energy dispersive spectrdmeter (EDS).

The loading amount of Pt was detected by inductively coupled plasma atomic emission spectrometry (ICP-AES) on the SpectroBlue instrument. A certain amount of sample was put into the sample tube, then a certain amount of aqua regia and HF were added dropwise successively, and then heated to dissolve. After dissolution,

the solution was poured into a volumetric flask, the remaining solution was washed with deionized water several times and added to the volumetric flask. Then a certain amount of 4% H_3BO_3 was added, and finally the volume was fixed in the volumetric flask. Aqua regia and 4% H_3BO_3 were prepared in advance.

The valence state of the catalysts were determined by X-ray photoelectron spectroscopy (XPS, Thermo Scientific ESCALAB 250Xi) with Al K_α X-ray source, the binding energy (BE) was calibrated using the C 1s peak (BE = 284.8 eV) of carbon contaminants.

The hydrogen temperature programmed reduction (H_2-TPR), hydrogen chemisorption, and toluene temperature programmed desorption (toluene-TPD) were tested by the Auto Chemisorb II 2920 instrument. In the H_2-TPR experiment, the catalyst was pretreated at 300 °C for 1 h under 5% O_2/He (30 mL/min) gas. After the temperature cooled down to 30 °C, the residual O_2 was removed at the flow of 10% H_2/Ar (30 mL/min) gas for 30 min, then the H_2-TPR curve was obtained by raising the temperature to 600 °C at the heating rate of 10 °C/min. In the hydrogen chemisorption experiment, the catalyst was pretreated at 400 °C for 1 h under 10% H_2/Ar (30 mL/min) gas, then the gas was switched to argon gas to purge the material. After the temperature cooled down to 30 °C and the baseline was flattened, pulses of 10% H_2/Ar gas were introduced to the sample until the peak area unchanged. In the toluene-TPD experiment, the catalyst was pretreated with 30 mL/min of 10% H_2/Ar gas at 300 °C for 1 h. Then, purged with helium gas to cool down to 50 °C, the gas was switched to 500 ppm toluene/N_2 gas for 60 min until the adsorption was saturated. Subsequently, the residual toluene gas was removed by purging with helium gas for 30 min. After the baseline was stabilized, the temperature was raised to 200 °C at the rate of 10 °C/min.

2.4. Catalytic combustion of toluene

A fixed bed reactor consisting of a quartz tube (inner diameter = 6 mm) was used to evaluate the toluene catalytic combustion activity. 0.1 g of the catalyst with the particle size of 40–60 mesh obtained by extrusion and sieving was placed in the middle of the tube reactor and fixed by quartz wool. The temperature of the catalyst was monitored by the thermocouple placed in the center of the reaction bed. Before the test, the catalyst was pretreated in a N_2 flow (50 mL/min) at 200 °C for 1 h. By bubbling synthetic air (21% O_2 + 79% N_2) through the carrier tank containing pure toluene and then further diluting it with another air stream to generate the inlet gas containing 1000 ppm toluene. The temperature of the carrier tank containing toluene was controlled by a condensing pump to stabilize the saturated vapor pressure of toluene. The total flow rate was kept at 100 mL/min, corresponding to the weight hourly space velocity (WHSV) was 60,000 mL g^{-1} h^{-1}. The toluene catalytic

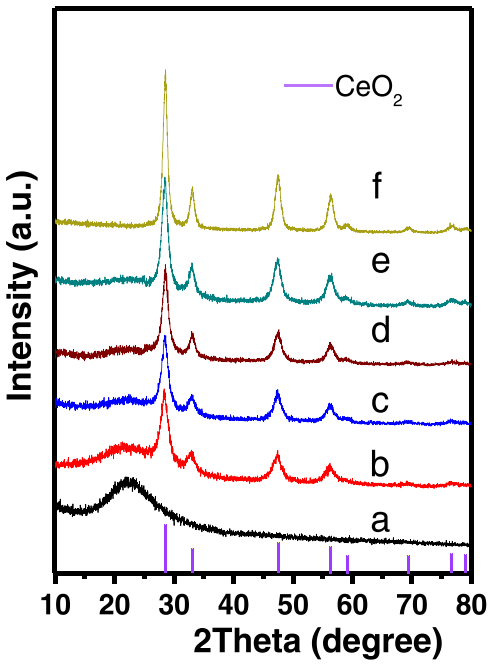

Fig. 1. XRD patterns of the samples: (a) NKM-5, (b) 20Ce/NKM-5, (c) 30Ce/NKM-5, (d) 40Ce/NKM-5, (e) 50Ce/NKM-5, and (f) CeO_2.

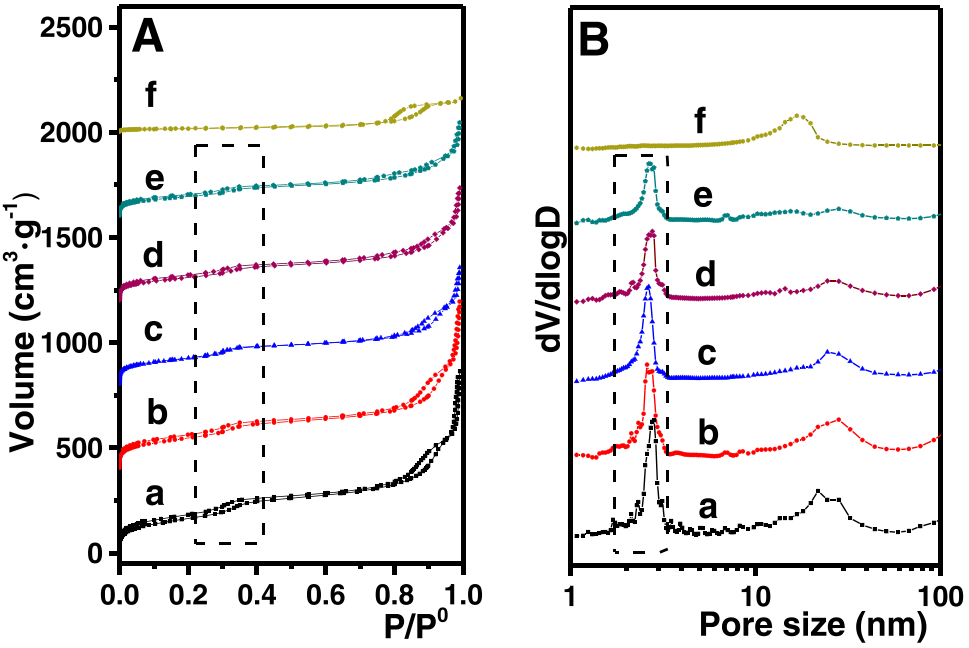

Fig. 2. (A) Nitrogen adsorption-desorption isotherms and (B) Pore size distribution curves of the samples: (a) NKM-5, (b) 20Ce/NKM-5, (c) 30Ce/NKM-5, (d) 40Ce/NKM-5, (e) 50Ce/NKM-5, and (f) CeO_2 (the adsorption-desorption isotherms for NKM-5, 20Ce/NKM-5, 30Ce/NKM-5, 40Ce/NKM-5, 50Ce/NKM-5, and CeO_2 were vertically shifted upward by 0, 400, 800, 1200, 1600, and 2000 cm^3 g^{-1}, respectively).

Table 1
The specific surface area, pore size, and pore volume of NKM-5, *x*Ce/NKM-5, and CeO_2 samples.

Sample	Specific surface area (m^2/g)	Mesopore size (nm)	Nanopore size (nm)	Pore volume (cm^3/g)	V_{meso} (cm^3/g)	V_{nano} (cm^3/g)
NKM-5	618	2.7	11–59	0.95	0.45	0.50
20Ce/NKM-5	505	2.7	13–52	0.77	0.37	0.40
30Ce/NKM-5	459	2.7	13–49	0.69	0.35	0.34
40Ce/NKM-5	407	2.7	18–47	0.61	0.32	0.29
50Ce/NKM-5	367	2.7	20–40	0.51	0.28	0.23
CeO2	64	–	8–28	0.23	–	0.23

activity tests were tested at the temperatures between 100 and 300 °C. The conversion of toluene was calculated based on the inlet and outlet concentration of toluene, CO_2 and H_2O were the only products in the catalytic combustion of toluene and the carbon content was basically the same for inlet and outlet gas.

The concentrations of toluene and CO_2 were analyzed by a SP-7890 gas chromatograph (China) equipped with two Flame Ionization Detectors (FID), where the concentration of toluene was tested using a FID with a SE-30 capillary column (30 m × 0.32 mm × 0.25 μm), the CO_2 concentration was measured by a FID with a TDX-01 column, a methanation furnace in front of the FID was installed. The conversion of toluene was calculated by the following Eq. (1):

$$\text{Toluene Conversion}(\%) = \frac{C_{Tol,in} - C_{Tol,out}}{C_{Tol,in}} \times 100\% \quad (1)$$

where $C_{Tol,\ in}$ and $C_{Tol,\ out}$ represent the concentration of toluene in the inlet gas and outlet gas, respectively.

In the test, the catalyst could be maintained at a stable temperature, each temperature point was maintained for about 1 h, the concentration of reactants and products were collected for several times at a certain temperature, and the average value was taken as the final result. In the repeatability test, the results of the catalyst could be repeated accurately.

The activation energy of the reaction was calculated at the conversion rate of toluene was less than 20% according to the following Arrhenius formula:

$$\ln r = -\frac{Ea}{RT} + \ln A \quad (2)$$

where r is the toluene oxidation rate (mol s^{-1} g_{Pt}^{-1}), Ea is the apparent activation energy (J mol^{-1}), R is the universal gas constant (J mol^{-1} K^{-1}), T is the catalyst temperature (K).

3. Results and discussion

3.1. Structural and morphological characterization

Fig. S1 shows the small-angle XRD of the NKM-5 sample, three obvious diffraction peaks of (200), (210), and (211) are attributed to the highly ordered cubic mesostructure of Pm3n [38]. Fig. 1 shows the wide-angle XRD of NKM-5, *x*Ce/NKM-5, and CeO_2 samples, 2θ at 22° corresponds to the amorphous silica peak of NKM-5, as the CeO_2 loading amount increased, the diffraction peak decreased gradually. The peak intensity of CeO_2 (JCPDS No.43-1002) increased gradually with the increase of CeO_2 loading amount, indicating that the CeO_2 nanoparticles has been successfully loaded on the NKM-5 support, and the CeO_2 crystal particles gradually grew up with the increase of loading amount. The CeO_2 crystallite sizes of 20Ce/NKM-5, 30Ce/NKM-5, 40Ce/NKM-5, 50Ce/NKM-5, and CeO_2 samples calculated by Scherrer equation are 4.3, 5.7, 6.5, 7.2, and 8.9 nm, respectively.

Fig. 2 shows the N_2 adsorption-desorption isotherms and pore size distribution curves of NKM-5, *x*Ce/NKM-5, and CeO_2 samples. It can be seen from Fig. 2A that the NKM-5 and *x*Ce/NKM-5 samples show type IV adsorption-desorption isotherms [39], it can be seen from Fig. 2B that the NKM-5 and *x*Ce/NKM-5 samples have mesopores concentrated at 2.7 nm and secondary pores distributed at 10–60 nm, the CeO_2 sample have stacked pores in the range of 8–28 nm. Table 1 shows the specific surface area, pore size distribution, and pore volume of NKM-5, *x*Ce/NKM-5, and CeO_2

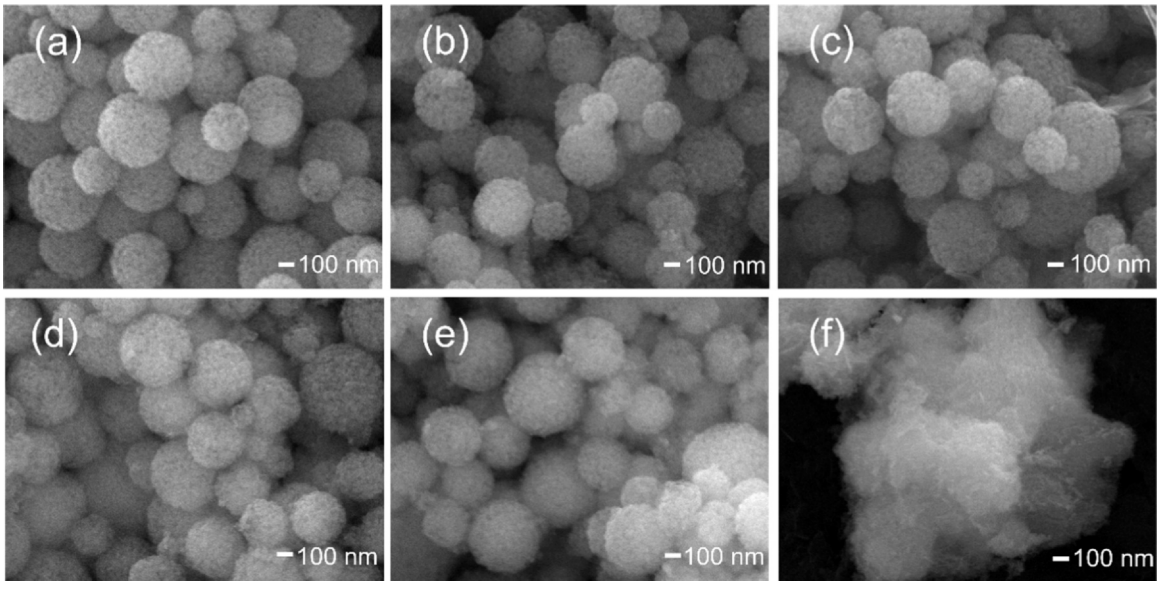

Fig. 3. SEM images of the samples: (a) NKM-5, (b) 20Ce/NKM-5, (c) 30Ce/NKM-5, (d) 40Ce/NKM-5, (e) 50Ce/NKM-5, and (f) CeO_2.

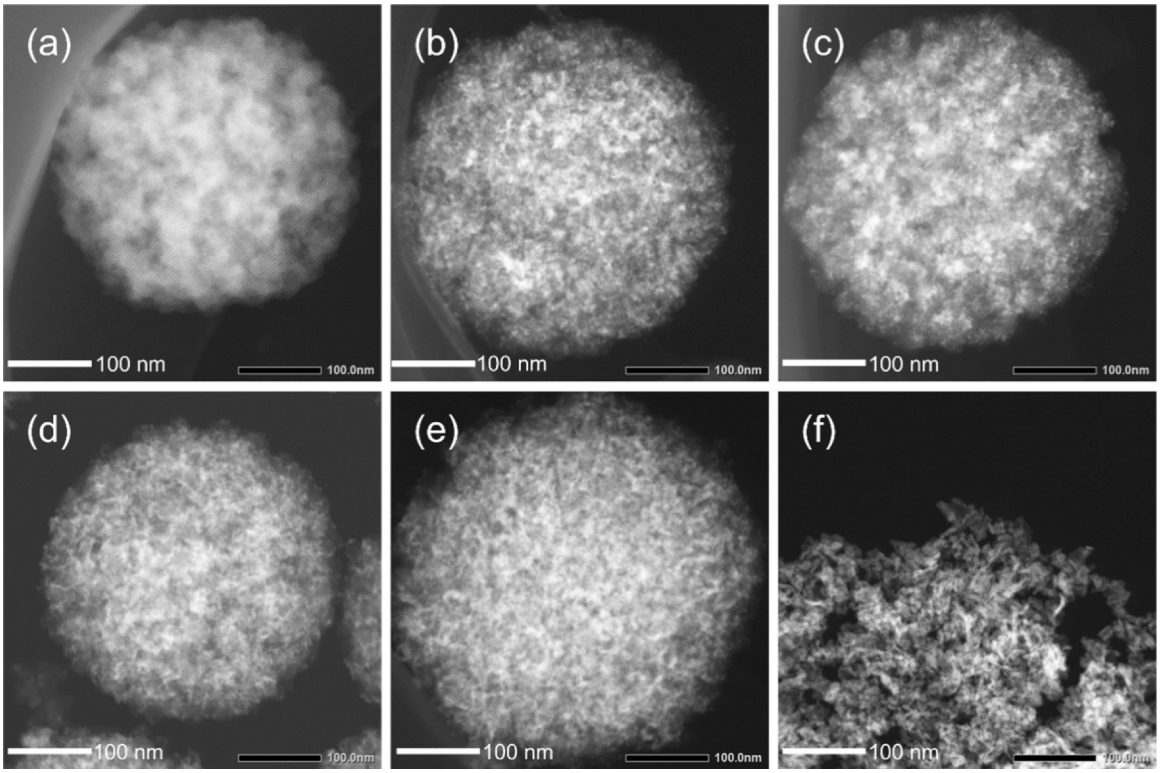

Fig. 4. STEM images of the samples: (a) NKM-5, (b) 20Ce/NKM-5, (c) 30Ce/NKM-5, (d) 40Ce/NKM-5, (e) 50Ce/NKM-5, and (f) CeO_2.

samples. It can be seen from Table 1 that the NKM-5 and *x*Ce/NKM-5 samples have excellent specific surface area and pore volume. With the increase of CeO_2 loading amount, the specific surface area, total pore volume, mesopore volume V_{meso}, and secondary nanopore volume V_{nano} all decreased gradually. Table S1 shows the specific surface area and pore volume of *x*Ce/NKM-5 samples normalized to gram of NKM-5, it can be seen from Table S1 that with the increase of CeO_2 loading amount, the specific surface area and pore volume of *x*Ce/NKM-5 decreased gradually. From the CeO_2 volume and unavailable volume, the pore volume decreased due to the CeO_2 blocked the pore volume and the pore volume accessibility decreased. It can also be seen from the Table 1 that the specific surface area and pore volume of the CeO_2 sample calcined by cerium nitrate are very low.

Fig. 3 and Fig. 4 show the SEM and STEM images of NKM-5, *x*Ce/NKM-5, and CeO_2 samples, it can be seen from Fig. 3a and Fig. 4a that the NKM-5 has the spherical morphology with the particle diameter of 200–500 nm and the hierarchical pore structure. After loading CeO_2 (Fig. 3b-e and Fig. 4b-e), the morphology of *x*Ce/NKM-5 sample is similar to that of NKM-5, indicating that the addition of CeO_2 did not destroy the morphology of NKM-5; the hierarchical pore structure became not obvious, which mainly due to the CeO_2 loaded blocked the pores. It can be seen from Fig. 3f and Fig. 4f that the pure CeO_2 sample has no regular morphology and the particles are also relatively large.

Using NKM-5, *x*Ce/NKM-5, and CeO_2 as supports, the Pt/NKM-5, Pt/*x*Ce/NKM-5, and Pt/CeO_2 catalysts were synthesized by impregnation method. Scheme 1 shows the synthesis process of Pt/*x*Ce/NKM-5 catalyst, the actual Pt loading amounts of Pt/NKM-5, Pt/20Ce/NKM-5, Pt/30Ce/NKM-5, Pt/40Ce/NKM-5, Pt/50Ce/NKM-5, and Pt/CeO_2 are 1.07, 1.04, 1.08, 1.03, 1.04, and 1.00 wt%, respectively. The actual Pt loading amounts of these catalysts are similar and consistent with the theoretical loadings. Fig. 5 shows the XRD patterns of Pt/NKM-5, Pt/*x*Ce/NKM-5, and Pt/CeO_2 catalysts. It can be seen from Fig. 5 that with the increase of CeO_2 loading amount, the diffraction peaks of Pt (2θ at 39.8°, 46.2°, and 67.5°) weakened gradually, indicating that the dispersion of Pt increased gradually [40]. The Pt particle sizes of Pt/NKM-5, Pt/20Ce/NKM-5, Pt/30Ce/NKM-5, and Pt/40Ce/NKM-5 catalysts calculated by Scherrer equation are 5.8, 4.9, 3.9, and 2.7 nm, respectively. The Pt diffraction peaks of Pt/50Ce/NKM-5 and Pt/CeO_2

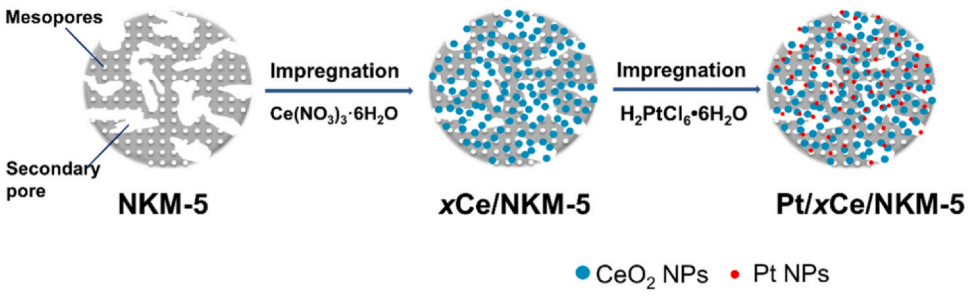

Scheme 1. The preparation procedure of Pt/*x*Ce/NKM-5 catalyst.

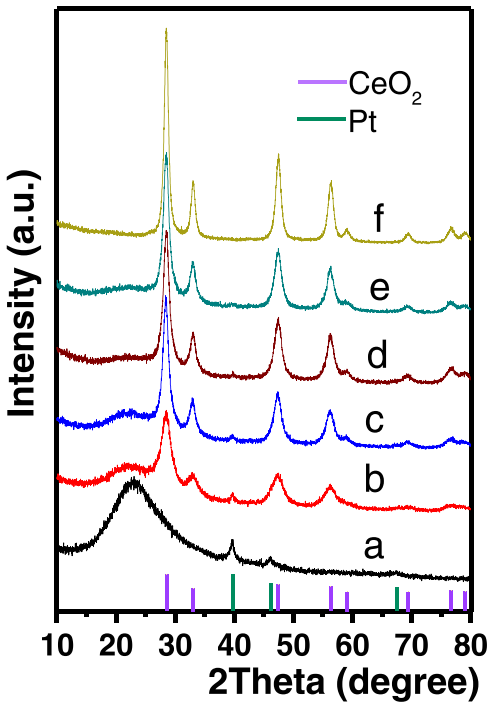

Fig. 5. XRD patterns of the catalysts: (a) Pt/NKM-5, (b) Pt/20Ce/NKM-5, (c) Pt/30Ce/NKM-5, (d) Pt/40Ce/NKM-5, (e) Pt/50Ce/NKM-5, and (f) Pt/CeO_2.

catalysts are too weak to be calculated, which means that they have more higher dispersion. The addition of CeO_2 could promote the dispersity of Pt and reduce the particle size of Pt nanoparticles.

Fig. 6 and Fig. S2 show the STEM and EDS elemental mapping of Pt/NKM-5, Pt/*x*Ce/NKM-5, and Pt/CeO_2 catalysts, it can be seen from Fig. 6a-c that the Pt/NKM-5 catalyst still keep the spherical morphology and the hierarchical pore structure, which indicates that loading Pt did not cause obvious damage to the NKM-5. However, the Pt nanoparticles are very obvious, and the Pt agglomeration is relatively serious, which is because the NKM-5 is an inert carrier and there is no interaction between Pt and NKM-5, the NKM-5 support can not stabilize and disperse Pt [24,25]. The morphology of Pt/*x*Ce/NKM-5 catalysts also did not change significantly after loading Pt, and there are no obvious Pt particles. EDS elemental mapping also shows that the Pt distribution is relatively uniform (Fig. 6d-f and Fig. S2), indicating that adding CeO_2 could promote the dispersion of Pt, which is consistent with the result of XRD. Fig. 6g-i shows the STEM and EDS elemental mapping of Pt/CeO_2 catalyst, there is no regular morphology, which is consistent with the SEM images. The Pt dispersities of Pt/NKM-5, Pt/20Ce/NKM-5, Pt/30Ce/NKM-5, Pt/40Ce/NKM-5, Pt/50Ce/NKM-5, and Pt/CeO_2 catalysts determined by hydrogen chemisorption are 26.3%, 43.6%, 48.7%, 51.5%, 74.8%, and 86.9%, respectively; the Pt surface areas are 0.65, 1.07, 1.20, 1.27, 1.84, and 2.14 m^2/g catalyst, respectively.

3.2. Chemical states and reduction property

Fig. 7 and Fig. S3 show the Pt 4f and Ce 3d XPS spectra of the Pt/NKM-5, Pt/*x*Ce/NKM-5, and Pt/CeO_2 catalysts. Fig. 7A shows the Pt 4f spectra of Pt/NKM-5 and Pt/*x*Ce/NKM-5 catalysts, Fig. S3A shows the Pt 4f spectra of Pt/CeO_2 catalyst, the peak at around 71.2 eV corresponds to the $4f_{7/2}$ peak of Pt^0, the peak at around 72.4 eV corresponds to the $4f_{7/2}$ peak of Pt^{2+}, and the peak at around 74.9 eV corresponds to the $4f_{7/2}$ peak of Pt^{4+} [25,41]. The ratios of $Pt^0/Pt^0+Pt^{2+}+Pt^{4+}$ are listed in the Table 2, the Pt mainly existed in the form of Pt^0 in the Pt/NKM-5 catalyst, with the increase of CeO_2 loading amount, the proportion of Pt^0 decreased gradually, and the proportion of $Pt^{2+}+Pt^{4+}$ increased gradually, which is because Pt loaded on the CeO_2 formed the Pt-O-Ce bond, with the increase of CeO_2 loading, the proportion of Pt loaded on the CeO_2 increased, and the metal-support interaction between Pt and CeO_2 increased [42]. According to the literature, Pt^0 has better catalytic combustion performance than Pt^{2+} and Pt^{4+} [43–45]. Fig. 7B shows the Ce 3d spectra of Pt/*x*Ce/NKM-5 catalyst, the u''' (916.9), v''' (898.6), u'' (907.7), v'' (889.9), u (901.1), and v (882.7) are classified as Ce^{4+} species, the u′ (903.7), v′ (885.8), u_0 (898.4), and v_0 (880.8) are classified as Ce^{3+} species [15,46,47], the proportions of $Ce^{3+}/Ce^{3+}+Ce^{4+}$ are listed in the Table 2. It can be seen from Table 2 that the ratio of Ce^{3+} increased gradually with the increase of CeO_2 loading, the generation of Ce^{3+} is attributed to the strong interaction between Pt and CeO_2; with the increase of CeO_2 loading amount, the Pt tended to be dispersed on the CeO_2, and more proportion of CeO_2 was loaded with Pt, and the higher concentration of Ce^{3+} indicates a higher concentration of oxygen vacancies [15,48–50].

Fig. 8 shows the H_2-TPR curves of the Pt/NKM-5 and Pt/*x*Ce/NKM-5 catalysts, Fig. S4 shows the H_2-TPR curves of the CeO_2 sample and the Pt/CeO_2 catalyst. It can be seen from Fig. S4 that the CeO_2 sample has two peaks at 380 °C and 487 °C, which are attributed to the reduction of surface oxygen and subsurface oxygen, respectively. After loading Pt, the Pt/CeO_2 catalyst has two peaks at 200 °C and 253 °C, the reduction temperature shifted to lower temperature, which is mainly because the interaction between Pt and CeO_2 lead to the formation of Pt-O-Ce bond, which could promote the low-temperature reducibility [51,52]. Fig. 8 shows that the Pt/NKM-5 catalyst has no reduction peak, after CeO_2 loaded, the Pt/*x*Ce/NKM-5 catalyst has a peak at 210 °C; the reduction peak shifted to lower temperature relative to the Pt/CeO_2 catalysts, which is because the NKM-5 support dispersed the CeO_2 nanoparticles, the interaction between Pt and CeO_2 was enhanced, and the Ce-O bond adjacent to Pt was easier to break, which enhanced the overflow of oxygen on the CeO_2 carrier surface and improved the reducibility of the catalyst. In addition, with the increase of CeO_2 loading amount, the hydrogen consumption increased gradually, and the reducibility increased gradually.

3.3. Catalytic activity

To investigate the hierarchical porosity of NKM-5, the commonly used mesoporous materials MCM-41 and SBA-15, and the NKM-5-0.3 sample with few secondary pores were used for comparison. The detailed preparation methods are shown in the Catalyst preparation. Fig. S5 shows the N_2 adsorption-desorption isotherms and pore size distribution of MCM-41, SBA-15, and NKM-5-0.3 samples, Table S2 shows the specific surface area, pore size distribution, and pore volume of the samples. It can be seen from Fig. S5 and Table S2 that MCM-41 and SBA-15 only have mesopores and no secondary pores, NKM-5-0.3 has mesopores and few secondary pores. The specific surface area and pore volume of the three samples are relatively excellent. Using MCM-41, SBA-15, and NKM-5-0.3 samples as carriers, Pt/MCM-41, Pt/SBA-15, and Pt/NKM-5-0.3 catalysts were synthesized by impregnation method. The Pt loadings of Pt/MCM-41, Pt/SBA-15 and Pt/NKM-5–0.3 catalysts are 1.03, 1.03, and 1.05 wt%, respectively. The Pt loading of the three catalysts is similar to that of Pt/NKM-5. Fig. S6 shows the XRD patterns of Pt/MCM-41, Pt/SBA-15, and Pt/NKM-5-0.3 catalysts. From the Fig. S6, it can be seen that the three catalysts have obvious Pt diffraction peaks. The Pt particle sizes of Pt/MCM-41, Pt/SBA-15, and Pt/NKM-5-0.3 catalysts calculated by

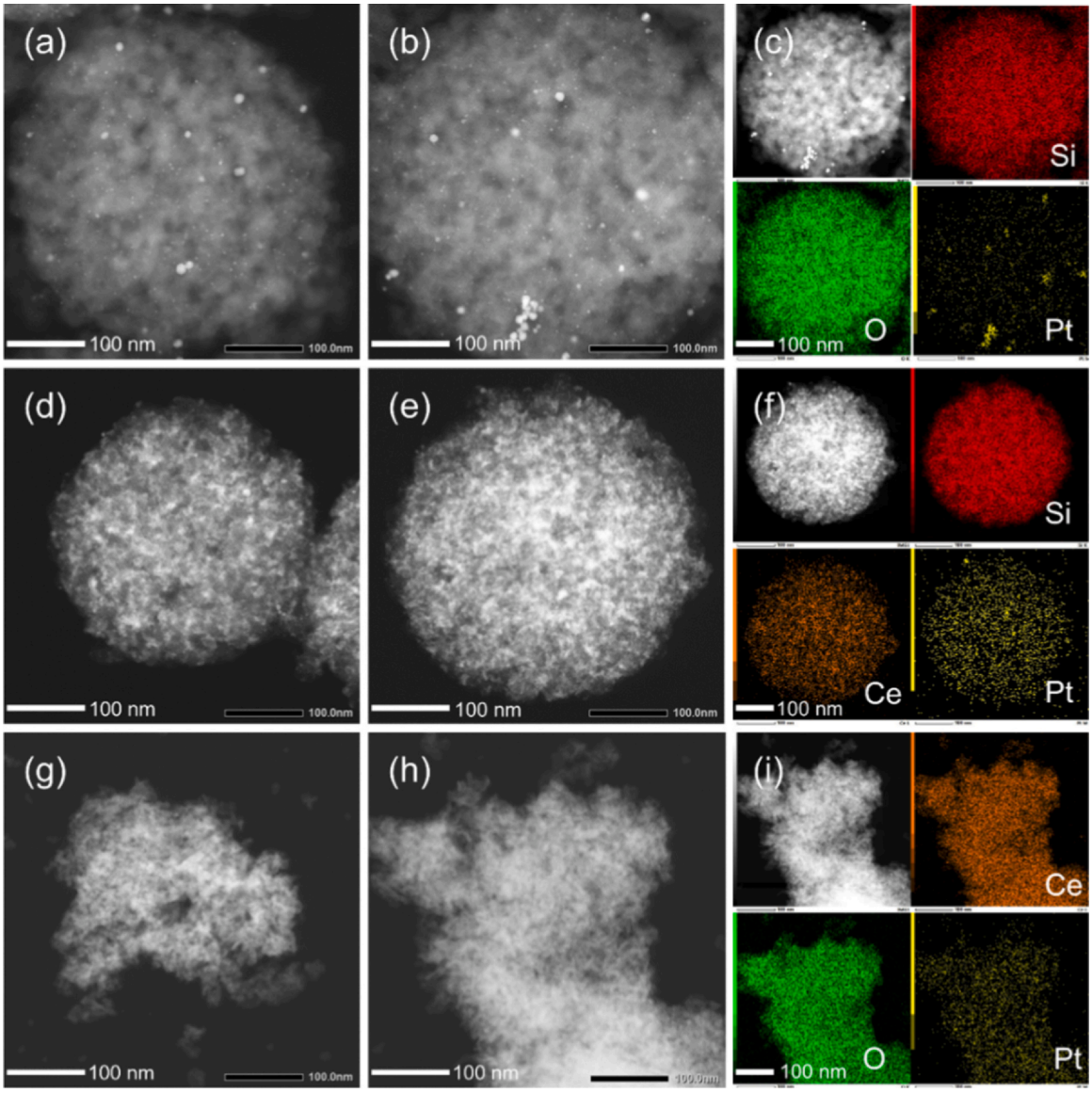

Fig. 6. STEM of the catalysts: (a) (b) Pt/NKM-5, (d) (e) Pt/30Ce/NKM-5, and (g) (h) Pt/CeO_2. EDS elemental mapping of the catalysts: (c) Pt/NKM-5, (f) Pt/30Ce/NKM-5, and (i) Pt/CeO_2.

Scherrer equation are 5.4, 4.8, and 6.0 nm, respectively, and the Pt particle size is similar to that of Pt/NKM-5. Fig. 9 shows the toluene catalytic combustion activity of Pt/NKM-5, Pt/MCM-41, Pt/SBA-15, and Pt/NKM-5–0.3 catalysts, Table S3 shows the T_{50} (the temperature at 50% conversion) and T_{90} (the temperature at 90% conversion) of the catalysts. From the Fig. 9 and Table S3, it can be seen that the Pt/NKM-5 catalyst has better catalytic activity than Pt/MCM-41, Pt/SBA-15, and Pt/NKM-5–0.3 catalysts, which is mainly due to the hierarchical pore structure of the NKM-5 sample, the hierarchical pore could promote the mass transport, reduce the diffusion path of reactants, improve the accessibility of active sites, and thus improve the catalytic performance [23,53,54].

Fig. 10A shows the toluene catalytic combustion activity of Pt/NKM-5, Pt/*x*Ce/NKM-5, and Pt/CeO_2 catalysts. It can be seen that the activities of the catalysts first increased and then decreased with the increase of CeO_2 loading amount. The Pt/30Ce/NKM-5 catalyst has the most excellent catalytic activity. Fig. 10B and Table 3 shows the T_{50} and T_{90} of the Pt/NKM-5, Pt/*x*Ce/NKM-5, and Pt/CeO_2 catalysts. It can be seen that both T_{50} and T_{90} first decreased and then increased with the increase of CeO_2 loading amount. The Pt/30Ce/NKM-5 catalyst has the lowest T_{50} and T_{90} temperatures, of which the T_{50} is 174 °C and the T_{90} is 195 °C. The activity first increased may be due to the addition of CeO_2 could enhance the metal-support interaction between Pt and CeO_2, promote the dispersion of Pt, and increase the reduction ability. When CeO_2 loading amount increased to a certain extent, the activity decreased may be due to the CeO_2 added reduced the specific surface area and pore volume, hindering the transfer of reactants and products, in addition, the active species Pt^0 also decreased. The excellent catalytic activity of Pt/30Ce/NKM-5 is attributed to the hierarchical pore structure of the support and the metal-support interaction between Pt and CeO_2. Besides, the activity of the catalysts in this work were compared with other catalysts in the literature, the results are listed in the Table S3, It can be seen from the Table S3 that the Pt/30Ce/NKM-5 catalyst has excellent catalytic activity. The reaction space velocity and particle size were adjusted to eliminate internal and external diffusion, and the kinetic measurement was performed under the conditions of

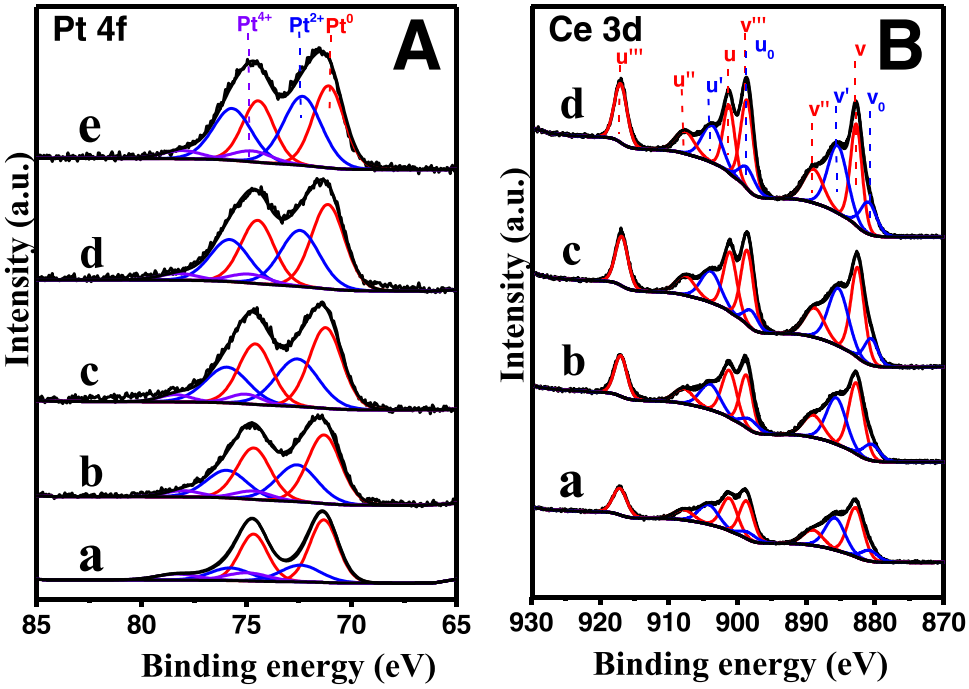

Fig. 7. (A) Pt 4f XPS spectra of the catalysts: (a) Pt/NKM-5, (b) Pt/20Ce/NKM-5, (c) Pt/30Ce/NKM-5, (d) Pt/40Ce/NKM-5, and (e) Pt/50Ce/NKM-5. (B) Ce 3d XPS spectra of the catalysts: (a) Pt/20Ce/NKM-5, (b) Pt/30Ce/NKM-5, (c) Pt/40Ce/NKM-5, and (d) Pt/50Ce/NKM-5.

Table 2
The ratios of $Pt^0/Pt^0+Pt^{2+}+Pt^{4+}$ and $Ce^{3+}/Ce^{3+}+Ce^{4+}$ of Pt/NKM-5, Pt/*x*Ce/NKM-5, and Pt/CeO_2 catalysts.

Catalyst	$Pt^0/Pt^0+Pt^{2+}+Pt^{4+}$	$Ce^{3+}/Ce^{3+}+Ce^{4+}$
Pt/NKM-5	0.64	–
Pt/20Ce/NKM-5	0.56	0.32
Pt/30Ce/NKM-5	0.54	0.34
Pt/40Ce/NKM-5	0.52	0.35
Pt/50Ce/NKM-5	0.46	0.36
Pt/CeO2	0.25	0.37

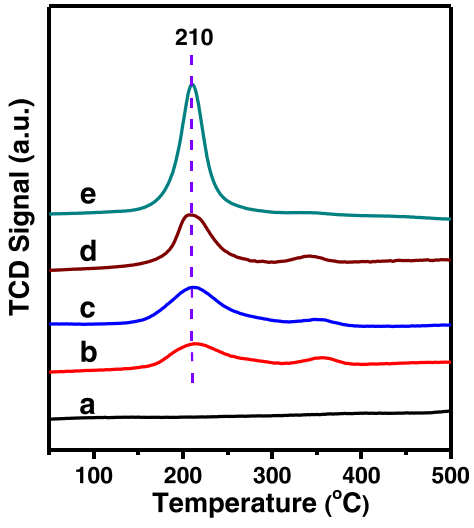

Fig. 8. H_2-TPR curves of the catalysts: (a) Pt/NKM-5, (b) Pt/20Ce/NKM-5, (c) Pt/30Ce/NKM-5, (d) Pt/40Ce/NKM-5, and (e) Pt/50Ce/NKM-5.

WHSV = 120,000 mL g^{-1} h^{-1} and size = 40–60 mesh, while keeping the conversion rate below 20% [55,56]. Fig. 10C shows the Arrhenius plots of toluene conversion reaction rate vs 1/T of Pt/NKM-5 and Pt/30Ce/NKM-5 catalysts. The activation energy of the Pt/NKM-5 and Pt/30Ce/NKM-5 catalysts are 149 and 104 kJ mol^{-1}, respectively. The activation energy of Pt/30Ce/NKM-5 is lower than that of Pt/NKM-5, which indicates that the toluene catalytic combustion reaction occurred more easily on the Pt/30Ce/NKM-5 catalyst. The stability test of Pt/30Ce/NKM-5 catalyst was performed at 190 °C, CO_2 was the only product detected and no other by-products were produced. The relationship between the catalytic activity of toluene and the reaction time is shown in Fig. 10D. It can be seen from Fig. 10D that the catalyst could maintain 80% conversion during 30 h of catalytic reaction, indicating that the catalyst has excellent stability.

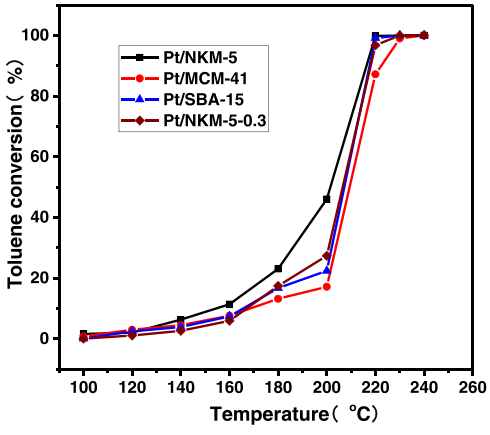

Fig. 9. Toluene catalytic combustion activity of Pt/NKM-5, Pt/MCM-41, Pt/SBA-15, and Pt/NKM-5-0.3 catalysts.

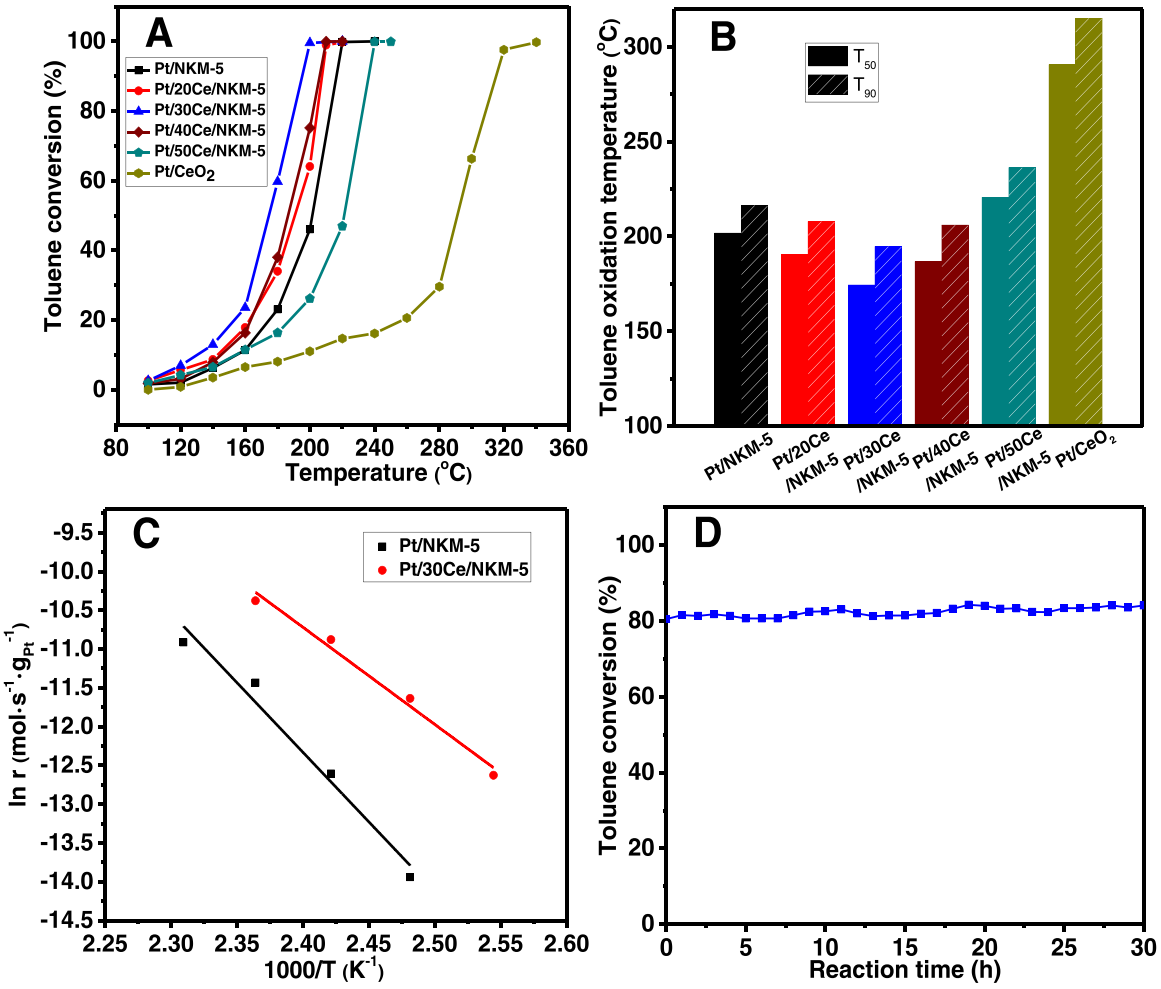

Fig. 10. (A) Toluene catalytic combustion activity of Pt/NKM-5, Pt/*x*Ce/NKM-5, and Pt/CeO_2 catalysts. (B) The T_{50} and T_{90} of the Pt/NKM-5, Pt/*x*Ce/NKM-5, and Pt/CeO_2 catalysts. (C) Arrhenius plots of reaction rate vs 1/T of Pt/NKM-5 and Pt/30Ce/NKM-5 catalysts. (D) Dependence of toluene catalytic combustion activity on reaction time over the Pt/30Ce/NKM-5 catalyst under the conditions of toluene concentration = 1000 ppm, mass space velocity = 60,000 mL g^{-1} h^{-1}, and reaction temperature = 190 °C.

Table 3
The Pt loading amount, Pt surface area, T_{50}, and T_{90} of Pt/NKM-5, Pt/*x*Ce/NKM-5, and Pt/CeO_2 catalysts.

Catalyst	Pt loading amount (wt%)	Pt surface area (m^2/g catalyst)	T_{50} (°C)	T_{90} (°C)
Pt/NKM-5	1.07	0.65	202	217
Pt/20Ce/NKM-5	1.04	1.07	191	208
Pt/30Ce/NKM-5	1.08	1.20	174	195
Pt/40Ce/NKM-5	1.03	1.27	187	206
Pt/50Ce/NKM-5	1.04	1.84	221	236
Pt/CeO2	1.00	2.14	291	315

Fig. 11 shows the toluene-TPD curves of Pt/NKM-5 and Pt/30Ce/NKM-5 catalysts. It can be seen that the desorption temperature of Pt/30Ce/NKM-5 catalyst is higher than Pt/NKM-5 catalyst, indicating that toluene bond more closely with Pt/30Ce/NKM-5, and the desorption peak area of Pt/30Ce/NKM-5 catalyst is larger than Pt/NKM-5, indicating that Pt/30Ce/NKM-5 catalyst has stronger toluene adsorption capacity than Pt/NKM-5 catalyst [57–59].

In addition to CeO_2, other oxides such as MnO_2 and TiO_2 have also been studied, the NKM-5 was used as the carrier to load different amounts of MnO_2 and TiO_2 to prepare *x*Mn/NKM-5 and *x*Ti/NKM-5 samples (*x* represents the MnO_2 or TiO_2 loading amount) by the impregnation method, and then supported Pt to prepare Pt/*x*Mn/NKM-5 and Pt/*x*Ti/NKM-5 catalyst by the impregnation method, the detailed preparation process of the catalysts are shown in the Catalyst preparation. Fig. S8 shows the XRD patterns of Pt/*x*Mn/NKM-5 and Pt/*x*Ti/NKM-5 catalysts. It can be seen that the diffraction peaks of MnO_2 (JCPDS No.24-0735) and TiO_2 (JCPDS No.21-1272) gradually increased, the Pt diffraction peaks decreased, indicating that the addition of MnO_2 and TiO_2 could promote the distribution of Pt, which is consistent with the results of the Pt/*x*Ce/NKM-5 catalyst. Fig. 12 and Table S4 show the toluene catalytic combustion activity of Pt/*x*Mn/NKM-5 and Pt/*x*Ti/NKM-5 catalysts. It can be seen from Fig. 12 and Table S4 that the Pt/40Mn/NKM-5 and Pt/30Ti/NKM-5 catalyst have the most excellent catalytic activity. From the results of Pt/*x*Ce/NKM-5, Pt/*x*Mn/NKM-5 and Pt/*x*Ti/NKM-5 catalysts, it could be concluded that adding a certain content of CeO_2, MnO_2, or TiO_2 could improve the activity of the Pt/NKM-5 catalyst.

4. Conclusions

The Pt/*x*Ce/NKM-5 catalyst was prepared by using the hierarchically porous silica NKM-5 as support and successively loading CeO_2 and Pt nanoparticles by the impregnation method. The NKM-5 support has mesopores (2.7 nm) and secondary pores (10–60 nm), and the specific surface area and pore volume are excellent. After CeO_2 loaded, the specific surface area and pore volume decreased

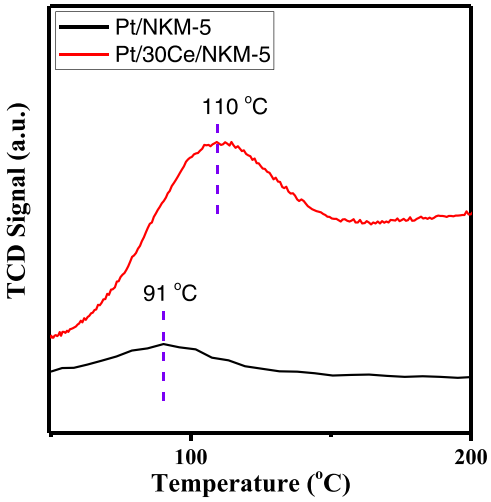

Fig. 11. Toluene-TPD curves of the Pt/NKM-5 and Pt/30Ce/NKM-5 catalysts.

gradually with the increase of CeO_2 loading amount. The dispersity of Pt nanoparticles is very poor in the Pt/NKM-5 catalyst, the Pt nanoparticles have a serious agglomeration phenomenon, after CeO_2 loaded, the dispersity of Pt nanoparticles was improved. With the increase of CeO_2 loading amount, the proportion of Pt^0 decreased gradually, the proportion of $Pt^{\delta+}$ increased gradually, the proportion of Ce^{3+} increased gradually, and the reducibility increased gradually, indicating that the metal-support interaction between Pt and CeO_2 increased gradually. As the CeO_2 loading amount increased, the metal-support interaction increased gradually, the dispersion of Pt and the reducibility of the catalyst increased gradually, which is beneficial to the catalytic reaction; but the specific surface area, pore volume, and the proportion of Pt^0 decreased, which is not conducive to catalytic reaction. The results of toluene catalytic combustion show that the Pt/30Ce/NKM-5 catalyst with a suitable loading has the most excellent catalytic performance.

CRediT authorship contribution statement

Yu Hao: Experiments, data analysis and paper writing. Shaohua Chen: Experiments and data analysis. **Luming Wu**: Experiments and data analysis. **Rui Chen**: XPS measurements and data analysis. **Pingchuan Sun**: Discussion and data analysis. **Tiehong Chen**: Discussion and paper writing.

Declaration of Competing Interest

The authors declare that they have no known competing financial interests or personal relationships that could have appeared to influence the work reported in this paper.

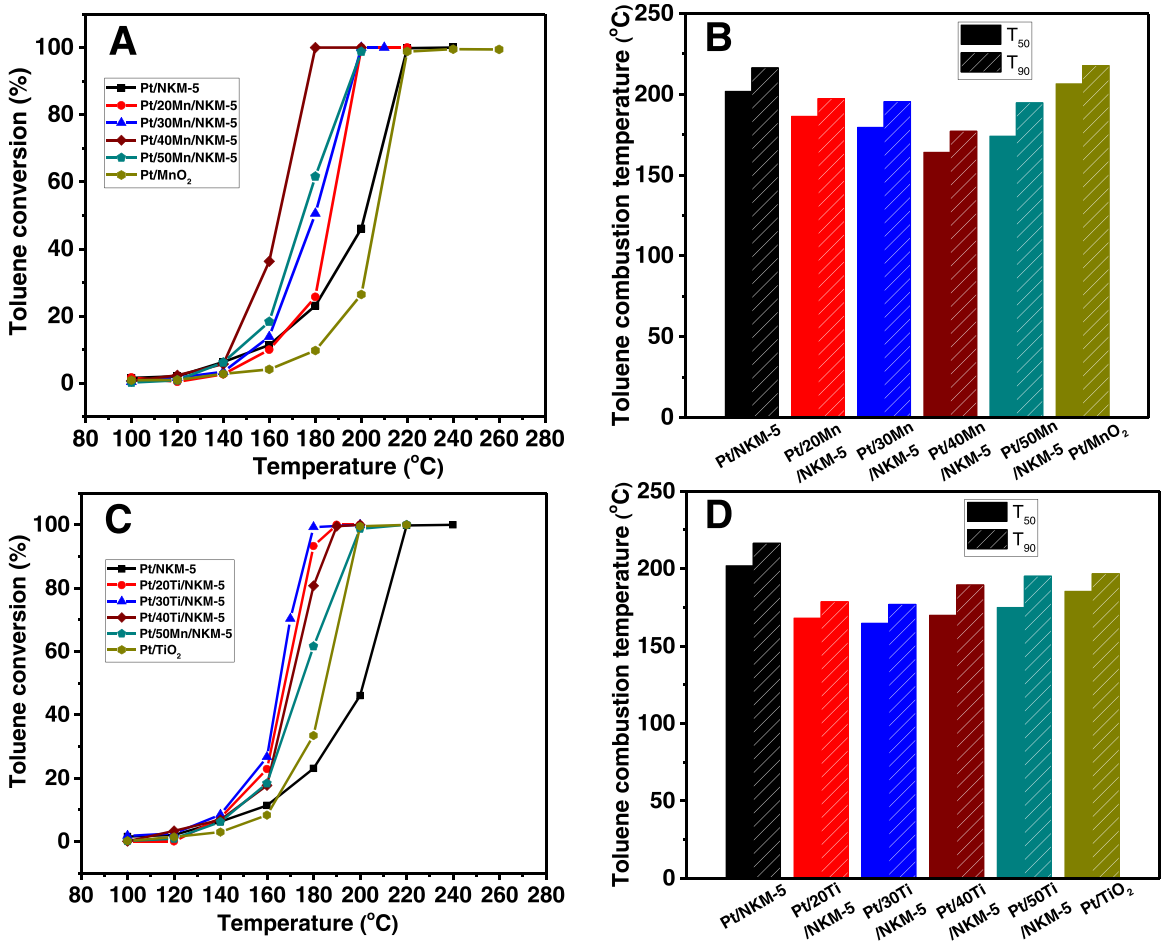

Fig. 12. (A) Toluene catalytic combustion activity of Pt/NKM-5, Pt/*x*Mn/NKM-5, and Pt/MnO_2 catalysts. (B) The T_{50} and T_{90} of the Pt/NKM-5, Pt/*x*Mn/NKM-5, and Pt/MnO_2 catalysts. (C) Toluene catalytic combustion activity of Pt/NKM-5, Pt/*x*Ti/NKM-5, and Pt/TiO_2 catalysts. (D) The T_{50} and T_{90} of the Pt/NKM-5, Pt/*x*Ti/NKM-5, and Pt/TiO_2 catalysts.

Acknowledgments

This work was supported by National Natural Science Foundation of China (21773128, 21534005, and 21421001).

Appendix A. Supporting information

Supplementary data associated with this article can be found in the online version at doi:10.1016/j.jallcom.2021.159030.

References

[1] C. Yang, G. Miao, Y. Pi, Q. Xia, J. Wu, Z. Li, J. Xiao, Abatement of various types of VOCs by adsorption/catalytic oxidation: a review, Chem. Eng. J. 370 (2019) 1128–1153.
[2] X.Y. Zhang, B. Gao, A.E. Creamer, C.C. Cao, Y.C. Li, Adsorption of VOCs onto engineered carbon materials: a review, J. Hazard. Mater. 338 (2017) 102–123.
[3] L.X. Zhong, F. Haghighat, Photocatalytic air cleaners and materials technologies-abilities and limitations, Build. Environ. 91 (2015) 191–203.
[4] Y. Li, S. Wu, J. Wu, Q. Hu, C. Zhou, Photothermocatalysis for efficient abatement of CO and VOCs, J. Mater. Chem. A 8 (2020) 8171–8194.
[5] W.-C. Chung, D.-H. Mei, X. Tu, M.-B. Chang, Removal of VOCs from gas streams via plasma and catalysis, Catal. Rev. 61 (2018) 270–331.
[6] Y. Guo, M. Wen, G. Li, T. An, Recent advances in VOC elimination by catalytic oxidation technology onto various nanoparticles catalysts: a critical review, Appl. Catal. B Environ. 281 (2021) 119447.
[7] Z. Su, W. Yang, C. Wang, S. Xiong, X. Cao, Y. Peng, W. Si, Y. Weng, M. Xue, J. Li, Roles of oxygen vacancies in the bulk and surface of CeO2 for toluene catalytic combustion, Environ. Sci. Technol. 54 (2020) 12684–12692.
[8] P. Yang, J. Li, Z. Cheng, S. Zuo, Promoting effects of Ce and Pt addition on the destructive performances of V2O5/γ-Al2O3 for catalytic combustion of benzene, Appl. Catal. A Gen. 542 (2017) 38–46.
[9] S. Huang, D. Yang, Q. Tang, W. Deng, L. Zhang, Z. Jia, Z. Tian, Q. Gao, L. Guo, Pt-loaded ellipsoidal nanozeolite as an active catalyst for toluene catalytic combustion, Microporous Mesoporous Mater. 305 (2020) 110292.
[10] G. Liu, Y. Tian, B. Zhang, L. Wang, X. Zhang, Catalytic combustion of VOC on sandwich-structured Pt@ZSM-5 nanosheets prepared by controllable intercalation, J. Hazard. Mater. 367 (2019) 568–576.
[11] S. Scirè, L.F. Liotta, Supported gold catalysts for the total oxidation of volatile organic compounds, Appl. Catal. B Environ. 125 (2012) 222–246.
[12] Y. Zeng, L. Gu, Y. Feng, W. Jiang, W. Ji, Morphologically uniform Pd/FexMn3−xO4-HP interfaces as the high-performance model catalysts for catalytic combustion of volatile organic compound, Appl. Surf. Sci. 528 (2020) 147006.
[13] S.C. Kim, W.G. Shim, Catalytic combustion of VOCs over a series of manganese oxide catalysts, Appl. Catal. B Environ. 98 (2010) 180–185.
[14] C. Chen, Q. Wu, F. Chen, L. Zhang, S. Pan, C. Bian, X. Zheng, X. Meng, F.-S. Xiao, Aluminium-rich Beta zeolite-supported platinum nanoparticles for the low-temperature catalytic removal of toluene, J. Mater. Chem. A 3 (2015) 5556–5562.
[15] R. Peng, X. Sun, S. Li, L. Chen, M. Fu, J. Wu, D. Ye, Shape effect of Pt/CeO2 catalysts on the catalytic oxidation of toluene, Chem. Eng. J. 306 (2016) 1234–1246.
[16] Z. Wang, P. Ma, K. Zheng, C. Wang, Y. Liu, H. Dai, C. Wang, H.-C. Hsi, J. Deng, Size effect, mutual inhibition and oxidation mechanism of the catalytic removal of a toluene and acetone mixture over TiO2 nanosheet-supported Pt nanocatalysts, Appl. Catal. B Environ. 274 (2020) 118963.
[17] J. He, D. Chen, N. Li, Q. Xu, H. Li, J. He, J. Lu, Controlled fabrication of mesoporous ZSM-5 zeolite-supported PdCu alloy nanoparticles for complete oxidation of toluene, Appl. Catal. B Environ. 265 (2020) 118560.
[18] L. Zhang, Y. Peng, J. Zhang, L. Chen, X. Meng, F.-S. Xiao, Adsorptive and catalytic properties in the removal of volatile organic compounds over zeolite-based materials, Chin. J. Catal. 37 (2016) 800–809.
[19] L. Zhang, Y. Jiang, B.-B. Chen, C. Shi, Y. Li, C. Wang, S. Han, S. Pan, L. Wang, X. Meng, F.-S. Xiao, Exceptional activity for formaldehyde combustion using siliceous Beta zeolite as a catalyst support, Catal. Today 339 (2020) 174–180.
[20] S. Zuo, X. Wang, P. Yang, C. Qi, Preparation and high performance of rare earth modified Pt/MCM-41 for benzene catalytic combustion, Catal. Commun. 94 (2017) 52–55.
[21] T. Dong, W. Liu, M. Ma, H. Peng, S. Yang, J. Tao, C. He, L. Wang, P. Wu, T. An, Hierarchical zeolite enveloping Pd-CeO2 nanowires: an efficient adsorption/catalysis bifunctional catalyst for low temperature propane total degradation, Chem. Eng. J. 393 (2020) 124717.
[22] J. Li, Y. Shi, X. Fu, J. Huang, Y. Zhang, S. Deng, F. Zhang, Hierarchical ZSM-5 based on fly ash for the low-temperature purification of odorous volatile organic compound in cooking fumes, React. Kinet. Mech. Cat. 128 (2019) 289–314.
[23] M.H. Sun, S.Z. Huang, L.H. Chen, Y. Li, X.Y. Yang, Z.Y. Yuan, B.L. Su, Applications of hierarchically structured porous materials from energy storage and conversion, catalysis, photocatalysis, adsorption, separation, and sensing to biomedicine, Chem. Soc. Rev. 45 (2016) 3479–3563.
[24] L. Deng, H. Miura, T. Shishido, S. Hosokawa, K. Teramura, T. Tanaka, Strong metal-support interaction between Pt and SiO2 following high-temperature reduction: a catalytic interface for propane dehydrogenation, Chem. Commun. 53 (2017) 6937–6940.
[25] K. Xi, Y. Wang, K. Jiang, J. Xie, Y. Zhou, H. Lu, Support interaction of Pt/CeO2 and Pt/SiC catalysts prepared by nano platinum colloid deposition for CO oxidation, J. Rare Earths 38 (2020) 376–383.
[26] Q. Wang, K.L. Yeung, M.A. Bañares, Ceria and its related materials for VOC catalytic combustion: a review, Catal. Today 356 (2019) 141–154.
[27] D. Kunwar, S. Zhou, A. DeLaRiva, E.J. Peterson, H. Xiong, X.I. Pereira-Hernández, S.C. Purdy, R. ter Veen, H.H. Brongersma, J.T. Miller, H. Hashiguchi, L. Kovarik, S. Lin, H. Guo, Y. Wang, A.K. Datye, Stabilizing high metal loadings of thermally stable platinum single atoms on an industrial catalyst support, ACS Catal. 9 (2019) 3978–3990.
[28] N.N. Mikheeva, V.I. Zaikovskii, G.V. Mamontov, Synthesis of ceria nanoparticles in pores of SBA-15: pore size effect and influence of citric acid addition, Micro Mesopor. Mat. 277 (2019) 10–16.
[29] T. Montini, M. Melchionna, M. Monai, P. Fornasiero, Fundamentals and catalytic applications of CeO2-based materials, Chem. Rev. 116 (2016) 5987–6041.
[30] K.M.S. Khalil, Cerium modified MCM-41 nanocomposite materials via a non-hydrothermal direct method at room temperature, J. Colloid Interf. Sci. 315 (2007) 562–568.
[31] X. Cheng, L. Huang, X. Yang, A.A. Elzatahry, A. Alghamdi, Y. Deng, Rational design of a stable peroxidase mimic for colorimetric detection of H2O2 and glucose: a synergistic CeO2/Zeolite Y nanocomposite, J. Colloid Interf. Sci. 535 (2019) 425–435.
[32] I. Maupin, J. Mijoin, J. Barbier, N. Bion, T. Belin, P. Magnoux, Improved oxygen storage capacity on CeO2/zeolite hybrid catalysts. Application to VOCs catalytic combustion, Catal. Today 176 (2011) 103–109.
[33] N. Li, J.G. Wang, J.X. Xu, J.Y. Liu, H.J. Zhou, P.C. Sun, T.H. Chen, Synthesis of hydrothermally stable, hierarchically mesoporous aluminosilicate Al-SBA-1 and their catalytic properties, Nanoscale 4 (2012) 2150–2156.
[34] J.-G. Wang, H.-J. Zhou, P.-C. Sun, D.-T. Ding, T.-H. Chen, Hollow carved single-crystal mesoporous silica templated by mesomorphous polyelectrolyte-surfactant complexes, Chem. Mater. 22 (2010) 3829–3831.
[35] C. Shi, G. Du, J. Wang, P. Sun, T. Chen, Polyelectrolyte-surfactant mesomorphous complex templating: a versatile approach for hierarchically porous materials, Langmuir 36 (2020) 1851–1863.
[36] D.Y. Zhao, J.L. Feng, Q.S. Huo, N. Melosh, G.H. Fredrickson, B.F. Chmelka, G.D. Stucky, Triblock copolymer syntheses of mesoporous silica with periodic 50 to 300 angstrom pores, Science 279 (1998) 548–552.
[37] Q. Zhang, F. Lü, C. Li, Y. Wang, H. Wan, An efficient synthesis of helical mesoporous silica nanorods, Chem. Lett. 35 (2006) 190–191.
[38] W.H. Fu, Y. Guan, Y.M. Wang, M.-Y. He, A facile synthesis of monodispersed mesoporous silica nanospheres with Pm3n structure, Micro Mesopor. Mat. 220 (2016) 168–174.
[39] B. Erdogan, H. Arbag, N. Yasyerli, SBA-15 supported mesoporous Ni and Co catalysts with high coke resistance for dry reforming of methane, Int. J. Hydrog. Energy 43 (2018) 1396–1405.
[40] X. Chen, J. Chen, Y. Zhao, M. Chen, H. Wan, Effect of dispersion on catalytic performance of supported Pt catalysts for CO oxidation, Chin. J. Catal. 33 (2012) 1901–1905.
[41] L.K. Ono, B. Yuan, H. Heinrich, B. Roldan Cuenya, Formation and thermal stability of platinum oxides on size-selected platinum nanoparticles: support effects, J. Phys. Chem. C 114 (2010) 22119–22133.
[42] M. Hatanaka, N. Takahashi, N. Takahashi, T. Tanabe, Y. Nagai, A. Suda, H. Shinjoh, Reversible changes in the Pt oxidation state and nanostructure on a ceria-based supported Pt, J. Catal. 266 (2009) 182–190.
[43] X. Fu, Y. Liu, W. Yao, Z. Wu, One-step synthesis of bimetallic Pt-Pd/MCM-41 mesoporous materials with superior catalytic performance for toluene oxidation, Catal. Commun. 83 (2016) 22–26.
[44] P. Zhao, X. Li, W. Liao, Y. Wang, J. Chen, J. Lu, M. Luo, Understanding the role of NbOx on Pt/Al2O3 for effective catalytic propane oxidation, Ind. Eng. Chem. Res. 58 (2019) 21945–21952.
[45] Q. Zhang, W. Su, P. Ning, X. Liu, H. Wang, J. Hu, Catalytic performance and mechanistic study of toluene combustion over the Pt-Pd-HMS catalyst, Chem. Eng. Sci. 205 (2019) 230–237.
[46] X. Liu, S. Jia, M. Yang, Y. Tang, Y. Wen, S. Chu, J. Wang, B. Shan, R. Chen, Activation of subnanometric Pt on Cu-modified CeO2 via redox-coupled atomic layer deposition for CO oxidation, Nat. Commun. 11 (2020) 4240.
[47] G. Chen, F. Rosei, D. Ma, Interfacial reaction-directed synthesis of Ce–Mn binary oxide nanotubes and their applications in CO oxidation and water treatment, Adv. Funct. Mater. 22 (2012) 3914–3920.
[48] Z. Jiang, M. Jing, X. Feng, J. Xiong, C. He, M. Douthwaite, L. Zheng, W. Song, J. Liu, Z. Qu, Stabilizing platinum atoms on CeO2 oxygen vacancies by metal-support interaction induced interface distortion: mechanism and application, Appl. Catal. B Environ. 278 (2020) 119304.
[49] B. Zhao, Y. Jian, Z. Jiang, R. Albilali, C. He, Revealing the unexpected promotion effect of EuO on Pt/CeO2 catalysts for catalytic combustion of toluene, Chin. J. Catal. 40 (2019) 543–552.
[50] S. Cai, D. Zhang, L. Zhang, L. Huang, H. Li, R. Gao, L. Shi, J. Zhang, Comparative study of 3D ordered macroporous Ce0.75Zr0.2M0.05O2−δ (M = Fe, Cu, Mn, Co) for selective catalytic reduction of NO with NH3, Catal. Sci. Technol. 4 (2014) 93–101.
[51] Y. Gao, W. Wang, S. Chang, W. Huang, Morphology effect of CeO2 support in the preparation, metal-support interaction, and catalytic performance of Pt/CeO2 catalysts, ChemCatChem 5 (2013) 3610–3620.
[52] R. Peng, S. Li, X. Sun, Q. Ren, L. Chen, M. Fu, J. Wu, D. Ye, Size effect of Pt nanoparticles on the catalytic oxidation of toluene over Pt/CeO2 catalysts, Appl. Catal. B Environ. 220 (2018) 462–470.
[53] P. Peng, X.-H. Gao, Z.-F. Yan, S. Mintova, Diffusion and catalyst efficiency in hierarchical zeolite catalysts, Natl. Sci. Rev. 7 (2020) 1726–1742.

[54] L.H. Chen, M.H. Sun, Z. Wang, W. Yang, Z. Xie, B.L. Su, Hierarchically structured zeolites: from design to application, Chem. Rev. 120 (2020) 11194–11294.
[55] Y. Hao, S. Chen, H. Wang, R. Chen, P. Sun, T. Chen, Platinum nanoparticles supported on hierarchically porous aluminosilicate nanospheres for low-temperature catalytic combustion of volatile organic compounds, ACS Appl. Nano Mater. 3 (2020) 8472–8482.
[56] B. Chen, B. Wu, L. Yu, M. Crocker, C. Shi, Investigation into the catalytic roles of various oxygen species over different crystal phases of MnO2 for C6H6 and HCHO oxidation, ACS Catal. 10 (2020) 6176–6187.
[57] Zhang, Yuan, Miao, Li, Shan, Jia, Zhang, Effect of Fe additives on the catalytic performance of ion-exchanged CsX zeolites for side-chain alkylation of toluene with methanol, Catalysts 9 (2019) 829.
[58] X. Zhou, X. Lai, T. Lin, J. Feng, Z. Hou, Y. Chen, Preparation of a monolith MnOx-CeO2/La-Al2O3 catalyst and its properties for catalytic oxidation of toluene, N. J. Chem. 42 (2018) 16875–16885.
[59] S. Huang, W. Deng, L. Zhang, D. Yang, Q. Gao, Z. Tian, L. Guo, T. Ishihara, Adsorptive properties in toluene removal over hierarchical zeolites, Microporous Mesoporous Mater. 302 (2020) 110204.